








Article

Reducing Non-Radiative Recombination Through Interfacial N-bromosuccinimide Engineering for Multi-Cation Perovskite Solar Cells

Hassen Dhifaoui ¹ , Pierre Colson ¹ , Gilles Spronck ¹ , Wajdi Belkacem ², Abdelaziz Bouazizi ², Guorui He ³ , Felix Lang ³ , Rudi Cloots ¹  and Jennifer Dewalque ^{1,*} 

¹ Group of Research in Energy and Environment from Materials (GREENMat), CESAM Research Unit, Chemistry Department, University of Liège, Allée du Six-Août 13, 4000 Liège, Belgium

² Group of Organic Electronic and Molecular Photovoltaics Devices, Laboratory of Condensed Matter and Nanosciences, Faculty of Sciences of Monastir, University of Monastir, Monastir 5019, Tunisia; belkacem.wajdi@gmail.com (W.B.)

³ Soft Matter Physics and Optoelectronics, Institute of Physics and Astronomy, University of Potsdam, Karl-Liebknecht-Str. 24-25, 14476 Potsdam-Golm, Germany

* Correspondence: jennifer.dewalque@uliege.be

Abstract

Minimizing surface defects in perovskite films is crucial for suppressing non-radiative recombination and enhancing device performance. Herein, we propose the use of N-bromosuccinimide (NBS), a small molecule containing Lewis base carbonyl groups (C=O), to improve the quality of RbCsMAFA mixed-cation perovskite films. This surface treatment effectively reduces non-radiative charge-carrier recombination, in particular through the passivation of surface defects related to undercoordinated Pb²⁺ ions and halide vacancies, and significantly accelerates charge extraction from the perovskite into the Spiro-OMeTAD hole transporter. Consequently, NBS-treated PerSCs achieve a power conversion efficiency (PCE) of 18.24%, representing an 11% relative increase over the control device (16.48%). This enhancement is mainly attributed to a V_{oc} gain of up to 40 mV and modifications in the recombination dynamics. Supporting evidence from impedance spectroscopic analyses further confirms enhanced energy-level alignment and reduced interfacial losses, improved charge transport as well as prolonged charge lifetimes within the devices. This work provides a simple yet effective approach to reduce the non-radiative recombination losses towards more efficient and stable PerSCs.

Keywords: interface engineering; quadruple cation perovskite; N-bromosuccinimide; defect passivation; non-radiative recombination



Academic Editor: Alessandro Latini

Received: 17 September 2025

Revised: 2 October 2025

Accepted: 7 October 2025

Published: 11 October 2025

Citation: Dhifaoui, H.; Colson, P.; Spronck, G.; Belkacem, W.; Bouazizi, A.; He, G.; Lang, F.; Cloots, R.; Dewalque, J. Reducing Non-Radiative Recombination Through Interfacial N-bromosuccinimide Engineering for Multi-Cation Perovskite Solar Cells. *Coatings* **2025**, *15*, 1195. <https://doi.org/10.3390/coatings15101195>

Copyright: © 2025 by the authors. Licensee MDPI, Basel, Switzerland. This article is an open access article distributed under the terms and conditions of the Creative Commons Attribution (CC BY) license (<https://creativecommons.org/licenses/by/4.0/>).

1. Introduction

Mixed-cation organolead halide perovskite solar cells (PerSCs) represent a promising third-generation photovoltaic technology, achieving remarkable progress in power conversion efficiency (PCE), which has surged from an initial 3.8% to over 26% [1–5]. This advancement is driven by the outstanding optoelectronic properties of perovskite materials, including tunable direct bandgap, high charge-carrier mobility, long carrier diffusion length, high absorption coefficient, and good defect tolerance [6–8]. Together with facile solution processability, flexibility, semi-transparency, and low-cost fabrication, these features make PerSCs as highly promising and attractive alternatives to conventional silicon photovoltaics [9]. Notably, interfacial energy loss caused by halide ion migration

and non-radiative recombination presents a critical bottleneck to further enhancing the photovoltaic efficiency and long-term stability of PerSCs, which still pose challenges for industrial commercialization [10–12]. One of the main factors underlying this issue is the presence of structural defects at the perovskite surface and grain boundaries, which act as preferential sites for unwanted degradation reactions [13]. In particular, defect states such as undercoordinated Pb^{2+} ions and halide vacancies can trap free charge carriers in perovskite films, thereby facilitating non-radiative recombination losses [14,15]. This not only leads to significant losses in open-circuit voltage (V_{oc}) and power conversion efficiency (PCE) but also diminishes carrier lifetimes in the devices. Moreover, such defects form preferential pathways for moisture and oxygen infiltration, which accelerates the decomposition of perovskite crystals, and all of this is detrimental to the long-term operational stability of photovoltaic devices [16]. Therefore, it is important to control the perovskite interface and adequately passivate the surface defects to reduce charge recombination and enhance device performance. So far, various materials, including metal oxides [17,18], polymers [19–21], and small organic molecules [22–25] have been employed as interfacial layers at the perovskite/hole transport layer (HTL) interface. For example, a series of organic ammonium halide salts, such as 4-tert-butylbenzylammonium iodide (tBBAI), was developed by the Grätzel group to effectively passivate surface defects in CsMAFA triple cation perovskites. Their studies demonstrated that incorporating tBBAI at the perovskite surface enhances charge extraction into the Spiro-OMeTAD hole transport layer, while simultaneously suppressing non-radiative recombination of charge carriers [26]. Naveen et al. systematically investigated the incorporation of two-dimensional metal dichalcogenides as interfacial materials at the perovskite/HTL interface, demonstrating their ability to substantially reduce trap density and effectively mitigate interfacial losses [27]. In addition, Daem et al. used tetracene to simultaneously control the lead-free $\text{Cs}_2\text{AgBiBr}_6$ double perovskite crystallization and suppress non-radiative recombination, leading to an improved PCE values [28]. Previous reports have established that the molecular additives containing functional Lewis base groups, such as $\text{C}=\text{O}$, can coordinate with uncoordinated Pb^{2+} in the perovskite, significantly increasing the electron density around lead sites due to the electron-donating effect of oxygen [29–31]. Inspired by these previous works, we report here that the use of N-bromosuccinimide (NBS) can passivate surface defects in the RbCsMAFA quadruple cation perovskite. Low-cost NBS is a chemical reagent commonly utilized as a bromine source and frequently employed in organic chemistry for various substitution and bromination reactions, and its two electron-withdrawing carbonyl groups facilitate the formation of reactive succinimide and bromine radicals [32,33]. In this study, its effects on the film quality and the device performance of PerSCs were systematically investigated. NBS molecules not only interact with uncoordinated Pb^{2+} ions on the surface of RbCsMAFA perovskite film, but also occupy halide vacancies via nitrogen-bromine bonding. This treatment lowers surface defect density, suppresses non-radiative recombination, and enhances charge transfer properties, resulting in a PCE increase from 16.48% to 18.24%, along with improved open-circuit voltage (V_{oc}) and fill factor (FF). These results were supported by the impedance and Mott-Schottky measurements of the devices. Our work offers a comprehensive analysis of the effect of NBS interfacial molecules on the optoelectronic properties and charge dynamics in multi-cation PerSCs, as well as their potential as a protective layer against moisture and oxygen. We established an evident relation between defect passivation, energy band alignment, photovoltaic (PV) performance, and recombination losses in the PerSCs, paving the way for further advancements in high-efficiency and stable devices.

2. Materials and Methods

Materials: Materials used in the experiment include Fluorine-doped tin oxide (FTO) glass (Greatcell Solar, Queanbeyan, NSW, Australia), Hydrochloric acid (HCl, 37%, VWR, Leuven, Belgium), Zinc powder (Zn, $\geq 98\%$, Carl Roth, Karlsruhe, Germany), Titanium diisopropoxide bis(acetylacetonate) (TAA, 75 wt.% in isopropanol, Sigma-Aldrich, Merck Life Science BV, Hoeilaart, Belgium), Anhydrous ethanol (EtOH, 99.5%, Acros organics, Geel, Belgium), Titanium(IV) chloride (TiCl_4 , $\geq 97.0\%$, Merck, Merck Life Science BV, Hoeilaart, Belgium), TiO_2 nanoparticle paste 18NR-T (Greatcell Solar), Cesium iodide (CsI, 99.9%, Sigma Aldrich), Rubidium iodide (RbI, 99.9%, Sigma Aldrich), Lead iodide (PbI_2 , 99%, Sigma Aldrich), Lead (II) bromide (PbBr_2 , $\geq 98\%$, Sigma Aldrich), Formamidinium iodide (FAI, 99.99%, Greatcell Solar), Methylammonium bromide (MABr, 99.99%, Greatcell Solar), N-Bromosuccinimide (NBS, 99%, Sigma Aldrich), 4-tert-butylpyridine (tBP, 96%, Sigma-Aldrich), Lithium bis(trifluoromethanesulfonyl)imide (Li-TFSI, 99.95%, Sigma-Aldrich), 2,20,7,70-Tetrakis[N,N-di(4-methoxyphenyl)amino]-9,90-spirobifluorene (Spiro-OMeTAD, $>99.9\%$, Borun, Ningbo, Zhejiang, China), N,N'-dimethylformamide (DMF, 99.9%, Acros organics), Dimethyl sulfoxide (DMSO, 99.9%, Sigma Aldrich), Anhydrous chlorobenzene (CB, 99.8%, Sigma Aldrich), Acetonitrile (ACN, 99.8% Sigma Aldrich), Anhydrous isopropanol (IPA, 99.8%, Acros organics). All materials were used as received without further purification.

Device fabrication: FTO glass substrates were initially etched using 2 M hydrochloric acid (HCl) with metallic zinc powder, followed by sequential ultrasonication in deionized water, acetone, and isopropanol for 20 min each, and then dried with compressed air. The FTO substrates were treated by UV-ozone cleaner for 15 min prior to deposition of the compact titanium dioxide (c- TiO_2) layer. The c- TiO_2 layer was deposited on the FTO substrates using spin-coating method from a precursor solution containing 0.243 mL acetylacetone and 0.366 mL titanium diisopropoxide bis(acetylacetonate) dissolved in 5 mL of extra-dry ethanol. The coated substrates were first annealed at 150 °C for 10 min on a hot plate in ambient air, followed by calcination at 500 °C for 30 min to form crystalline anatase TiO_2 . After cooling to room temperature, the samples underwent an additional 15 min of UV-ozone treatment. The mesoporous titanium dioxide (mp- TiO_2) solution was prepared by diluting 1 g of TiO_2 18NR-T paste in 9.8 g of extra-dry ethanol. This solution was spin-coated atop the c- TiO_2 layer at 1500 rpm for 30 s, followed by annealing at 150 °C for 10 min and calcination at 500 °C for 30 min. Following this, the samples were immersed in a 0.04 M aqueous TiCl_4 solution for 30 min at 60 °C, rinsed sequentially with deionized water and ethanol, dried with compressed air, and finally calcined at 450 °C for 30 min. After cooling, a final 15 min of UV-ozone treatment was applied before transferring the substrates into an Argon-filled glovebox with controlled oxygen and moisture levels. The quadruple cation $\text{RbCsMAFAPbI}_{3-x}\text{Br}_x$ perovskite precursor solution (1.5 M) was prepared by dissolving 0.6 g FAI, 2.2 g of PbI_2 , 0.1 g of MABr, 0.5 g of PbBr_2 , 0.5 g of CsI, and 0.5 g of RbI in a mixed solvent of DMF and DMSO with 4:1 volume ratio. The filtered perovskite solution was spin-coated onto the substrates at 1000 rpm for 15 s, 4000 rpm for 1 s, and 6000 rpm for 20 s, followed by 120 μL of chlorobenzene dripping in the last 10 s. The films were then annealed at 100 °C for 30 min to induce perovskite crystallization. For N-bromosuccinimide (NBS) passivation, solutions of 0.5, 1.0, 2.0, and 3.0 mg/mL in isopropanol were spin-coated at 3000 rpm for 30 s, followed by annealing at 100 °C for 8 min. The Spiro-OMeTAD hole transport solution was prepared by dissolving 72.3 mg of Spiro-OMeTAD in 1 mL chlorobenzene, with 18 μL Li-TFSI (520 mg mL^{-1} in acetonitrile) and 29 μL tBP as additives. This solution was deposited atop the NBS layer at 3000 rpm for 30 s. Finally, a 100 nm gold electrode was thermally evaporated under vacuum (8.5×10^{-6} mbar).

Characterization of films and devices: UV-Visible absorption spectra were measured by UV-VIS-NIR spectrophotometry on a Shimadzu (Shimadzu Benelux, s-Hertogenbosch,

The Netherlands) 3600 Plus instrument with an integrating sphere (ISR1503). X-ray diffraction (XRD) was collected on a X-ray diffractometer (Bruker D8, Karlsruhe, Germany) with monochromatic $\text{CuK}\alpha$ radiation. The scanning electron microscopy (SEM) images were obtained with a field-emission gun microscope TESCAN CLARA (Brno, Czech Republic) under a 15-kV accelerating voltage. The hydrophobicity of the films was assessed by measuring the contact angle of a water droplet on the film surface by using a contact angle goniometer (KSV CAM 200, technex bv, Zaanstad, The Netherlands). The X-ray photoelectron spectroscopy (XPS) measurements were performed using a Thermo Scientific (Waltham, MA, USA) K-Alpha spectrometer with monochromatic $\text{AlK}\alpha$ radiation. Photoluminescence (PL) measurements were conducted using a 520 nm continuous-wave laser (In-saneware), which was coupled into an integrating sphere via an optical fiber. The laser intensity was calibrated to a 1 sun equivalent by matching the short-circuit current of a 1 cm^2 perovskite solar cell (22.0 mA/cm^2). Emission from the samples was collected through a second optical fiber and directed into an Andor (Belfast, Northern Ireland) SR393iB spectrometer equipped with a silicon CCD (DU420A-BR-DD, iDus). System calibration was performed using a halogen lamp with a known spectral irradiance, and a spectral correction factor was applied to align the detector response with the lamp calibrated output. The spectral photon density was then obtained by dividing the corrected detector signal (spectral irradiance) by the photon energy ($h\nu$), and the total photon numbers for both excitation and emission were determined through numerical integration using MATLAB (V R2025a). The current density–voltage characteristics of the cells were measured by a class A solar simulator (Newport Spectra Physics, Utrecht, The Netherlands) coupled to a Keithley 2400 (Newport Spectra Physics, Utrecht, The Netherlands) source meter under AM 1.5 G (100 mW cm^{-2}) with a 0.0355 cm^2 aperture black mask. A silicon photodiode was used as the light intensity calibrator for each measurement. Electrochemical impedance spectroscopy (EIS) measurements were carried out using BioLogic (Seyssinet-Pariset, France) SP-200 Potentiostat using a sinusoidal potential perturbation of 10 mV, over the frequency range from 3 MHz to 1 mHz, at room temperature. Data were fitted using EC Lab software (V11.62.5).

3. Results and Discussion

To investigate the influence of NBS treatment on the RbCsMAFA quadruple cation perovskite layer, thin films of NBS at varying concentrations (0.5, 1.0, 2.0, and 3.0 mg/mL) were deposited atop the perovskite. Initially, we conducted UV-Visible absorption spectra measurements. As shown in Figure 1a, the light absorption intensity of the perovskite gradually increases with NBS addition, while varying the NBS content does not significantly affect the optical absorption in the 450–850 nm range for pristine NBS films (Figure S1). The increase in overall absorption intensity observed in Figure 1a therefore likely reflects combined effects of improved film morphology and reduced defect-related losses, rather than a direct optical effect of NBS. Importantly, the absorption edge of the perovskite redshifts as the NBS concentration increases. The bandgaps of the NBS-treated perovskite samples were measured using Tauc plot analysis (Figure S2), and we found that the optical bandgap decreases with increasing NBS concentration. This decrease in bandgap means that the NBS-treated perovskite can absorb lower-energy photons, generate more photocarriers, and thereby enhance the photocurrent of PerSCs [7].

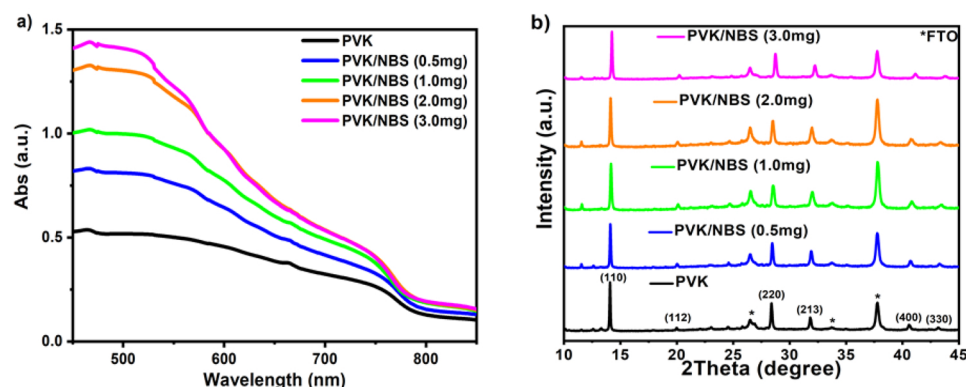


Figure 1. (a) UV–visible absorption spectra, and (b) X-ray diffraction patterns of the pristine RbCsMAFA perovskite (PVK) films and with varying NBS concentration (0.5 mg/mL, 1.0 mg/mL, 2.0 mg/mL, and 3.0 mg/mL).

In addition, X-ray diffraction (XRD) measurements were performed to further investigate the crystallinity effect of NBS on the quadruple cation perovskite films (Figure 1b). The XRD patterns of perovskite films with and without NBS revealed similar diffraction peaks, with the characteristic peaks at 14.06° , 19.97° , 28.35° , and 31.84° corresponding to the (110), (112), (220), and (213) planes of the RbCsMAFA perovskite structure, consistent with previous reports [3,34]. We found that NBS treatment increases the XRD peak intensity, reaching a maximum for the sample prepared with 2.0 mg/mL NBS, suggesting that optimal NBS incorporation promotes superior crystallinity and improved structural coherence in the perovskite films. Simultaneously, the diffraction peaks shift toward higher 2θ values, indicative of lattice contraction due to Br^- ions partially occupying halide vacancies. Such peak shifts are commonly observed in bromide-modified perovskites and have been associated with lattice stabilization and reduced ion migration in previous studies [35,36]. The surface morphologies of perovskite films, both untreated and treated with NBS, were examined using scanning electron microscopy (SEM). The perovskite films treated with NBS exhibit smoother and more compact morphology surface with fewer grain boundaries compared to the control sample (Figure S3). In addition, with the NBS treatment, the water contact angle of the perovskite film increases from 59.23° to over 74° (Figure S4), which is beneficial to the moisture resistance of the perovskite layer for the improvement of device stability. This is attributed to the hydrophobic nature of the NBS molecules. Moreover, the photoluminescence (PL) spectra in Figure S5 show that the NBS-treated perovskite film exhibits significantly higher emission than the untreated film. This PL enhancement indicates reduced non-radiative recombination losses and, consequently, a lower defect density in the NBS-treated perovskite. In perovskite solar cells, trap states at surfaces and grain boundaries in the perovskite significantly contribute to non-radiative losses. By passivating these traps, NBS-treated films allow excited carriers to persist longer and recombine radiatively, increasing the PL signal. Similar observations have been reported in previous studies [37,38], where interfacial engineering led to stronger PL emission and improved device performance.

The enhanced structural and morphological quality of RbCsMAFA perovskite films can be directly attributed to the effective passivation of surface defects. To unveil the impact of NBS treatment on the surface chemical composition, X-ray photoelectron spectroscopy (XPS) analysis was conducted. The survey and high-resolution XPS spectra of the perovskite samples treated with different concentrations of NBS are shown in Figures S6 and S7. Figure 2a–g illustrate the core-levels XPS spectra of the pristine perovskite and perovskite treated with 2.0 mg/mL NBS. Figure 2a presents the C 1s spectra, where the pristine perovskite exhibits two XPS peaks at 284 eV (attributed to C–C bonds) and 287 eV (assigned

to C=O bonds). However, after being covered with NBS layer, the intensities of these signals increase, confirming the presence of NBS on the perovskite surface [39]. The N 1s spectra are shown in Figure 2b, where the pristine sample shows a single peak at 400.20 eV, assigned for $-\text{NH}_2$ groups, which is shifted by 0.2 eV to higher binding energy upon NBS treatment. This observed shift confirms the stronger hydrogen bond accepting ability of NBS [39,40]. Moreover, as depicted in Figure 2c, the main Pb 4f_{5/2} and Pb 4f_{7/2} peaks shift from 142.94 eV to 143.14 eV and from 138.08 eV to 138.28 eV, respectively, upon NBS treatment. This shift toward higher binding energies indicates an interaction between the functional carbonyl group (C=O) in the NBS molecule and undercoordinated Pb²⁺ ions through a coordination effect, effectively passivating these defect sites. Consequently, the density of trap states on the perovskite film surface is reduced, enhancing both the structural integrity of the [PbX₆]^{4−} octahedral framework and the overall stability of the 3D perovskite lattice [27,39]. Overall, the [Pb(I/Br)₆]^{4−} framework interacts with A-site cations through hydrogen bonding ($-\text{NH}_3^+$ groups), stabilizing the 3D perovskite structure [41]. The corresponding I 3d spectra (Figure 2d) exhibit a similar shift, with the main I 3d_{3/2} and I 3d_{5/2} peaks moving from 630.44 eV and 618.98 eV in the pristine perovskite to higher binding energies of 630.65 eV and 619.76 eV, respectively, for the NBS-treated perovskite. This shift suggests that NBS could modify the anionic defects (I-/Br-), and anti-sites. The nitrogen-bound bromine (N-Br) can release Br[−] ions, which may fill halide vacancies and further contribute to defect passivation. Thus, NBS is capable of passivating both cationic and anionic defect sites in the perovskite [42]. Furthermore, the O 1s signal (Figure 2e) of the pristine perovskite shows a peak at 532.14 eV, which significantly decreases in intensity after NBS addition. This reduction implies that the NBS layer effectively mitigates moisture and oxygen infiltration, thereby preventing oxidation pathways that typically initiate perovskite degradation. These findings are corroborated by contact angle measurements, which demonstrate enhanced surface hydrophobicity and reinforce the protective role of the NBS molecules. Furthermore, the increase in Br 3d peak intensity with increasing NBS concentration reflects an enrichment of surface bromide content (Figure 2f), likely arising from partial substitution of iodide by Br[−] released from NBS and the filling of halide vacancies [43,44].

In the meantime, the valence band spectra were determined by XPS, as shown in Figure 2g, from which we can derive the valence band maximum (VBM) of pristine perovskite and NBS-treated perovskite to be 0.76 eV and 0.63 eV below the Fermi level, respectively. This upward shift implies that the NBS treatment slightly modifies the band edge structure of the perovskite and reduces the energetic mismatch between the perovskite and Spiro-OMeTAD transport states. By lowering the hole extraction barrier at the HTL/perovskite interface (Figure 2h), NBS facilitates more efficient hole transfer, which can enhance interfacial charge separation and ultimately improve the photovoltaic performance of the device.

We then evaluated NBS as an interfacial layer in n-i-p perovskite solar cells with the following device architecture: FTO glass/c-TiO₂/mp-TiO₂/RbCsMAFA/NBS/Spiro-OMeTAD/Au (Figure 3a). The cross-sectional SEM image of the PerSC with NBS (Figure S8) reveals the thicknesses of the blocking and mesoporous TiO₂ layers (~180 nm), the perovskite layer (~300 nm), and the NBS interfacial and Spiro-OMeTAD hole transport layers (~200 nm). The typical current density-voltage (J-V) curves under standard AM 1.5 G illumination for the PerSCs with varying NBS concentrations are presented in Figure 3b, with their corresponding PV parameters summarized in Table 1 (average on 8 devices for each NBS concentration). The statistical distribution of photovoltaic parameters (V_{oc}, J_{sc}, PCE, and FF) of PerSCs, with and without NBS, are illustrated in Figure S10. We established an optimal NBS concentration of 2.0 mg/mL, at which the PCE reached 18.24%

with V_{oc} of 1.041 V, short-circuit current (J_{sc}) of 24.29 mA cm^{-2} , and FF of 71.31, while the NBS-untreated device has PCE of 16.48% (V_{oc} of 1.004 V, J_{sc} of 23.67 mA cm^{-2} , and FF of 69.30). It can be deduced that the NBS interfacial layer boosts the photovoltaic performance of PerSCs, mainly due to improved V_{oc} and FF. Meanwhile, lower hysteresis can also be observed in the NBS-treated PerSC (Figure S9), which is ascribed to the suppression of charge accumulation due to the reduction in surface defect states, and the promotion of energy level alignment (as demonstrated above). The reduction in the energy offset between the valence band maximum of RbCsMAFA perovskite and the highest occupied molecular orbital (HOMO) level of the HTL facilitates faster hole extraction and minimizes non-radiative recombination, which is also consistent with previous studies [45,46].

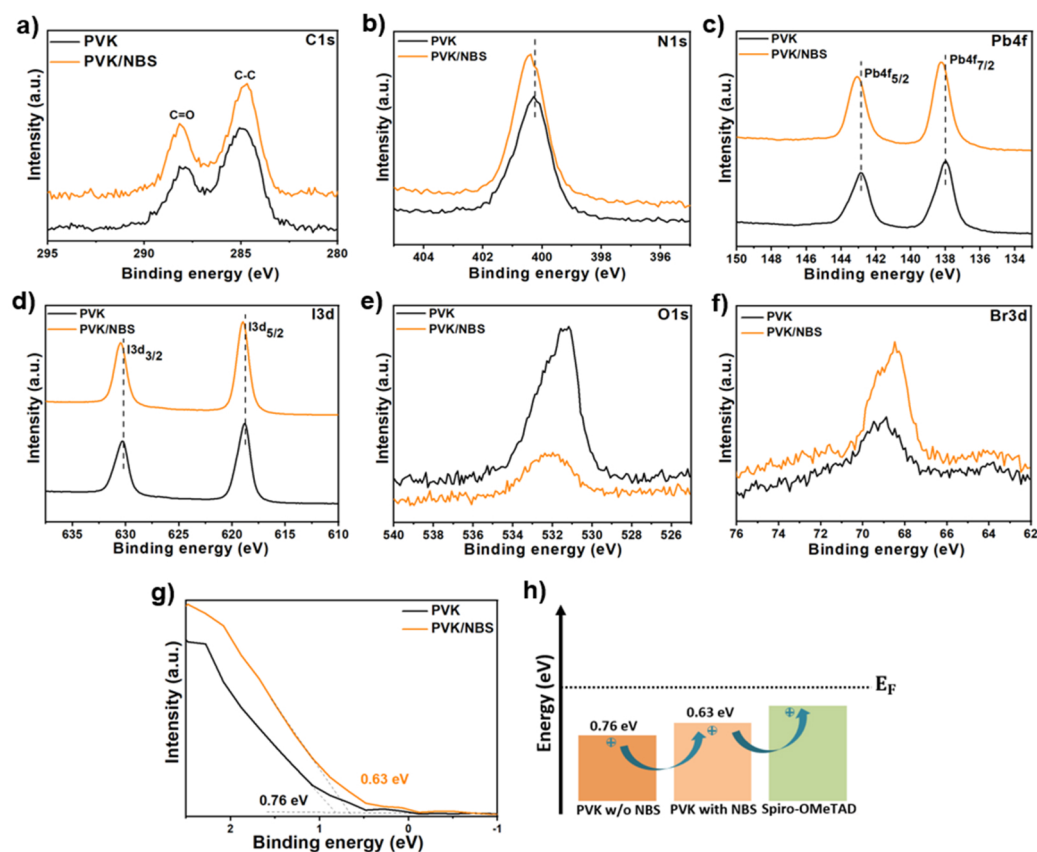


Figure 2. High-resolution X-ray photoelectron spectroscopy (XPS): (a) C 1s, (b) N 1s, (c) Pb 4f, (d) I 3d, (e) O 1s, (f) Br 3d core levels, and (g) valence band XPS spectra of the pristine perovskite and perovskite treated with 2.0 mg/mL NBS. (h) Schematic energy levels of perovskite vs. HTL, with and without NBS.

Table 1. Photovoltaic parameters of the PerSCs without and with NBS from varying NBS concentration: 0.5 mg/mL, 1.0 mg/mL, 2.0 mg/mL, and 3.0 mg/mL. Average values across 8 devices for each NBS concentration. Statistical distribution available in Figure S10.

PerSC	V_{oc} (V)	J_{sc} (mAcm^{-2})	FF (%)	PCE (%)
w/o NBS	1.004	23.67	69.30	16.48
with NBS (0.5 mg)	1.021	23.57	70.66	16.99
with NBS (1.0 mg)	1.032	24.16	70.77	17.79
with NBS (2.0 mg)	1.041	24.29	71.31	18.24
with NBS (3.0 mg)	1.041	23.96	71.22	18.17

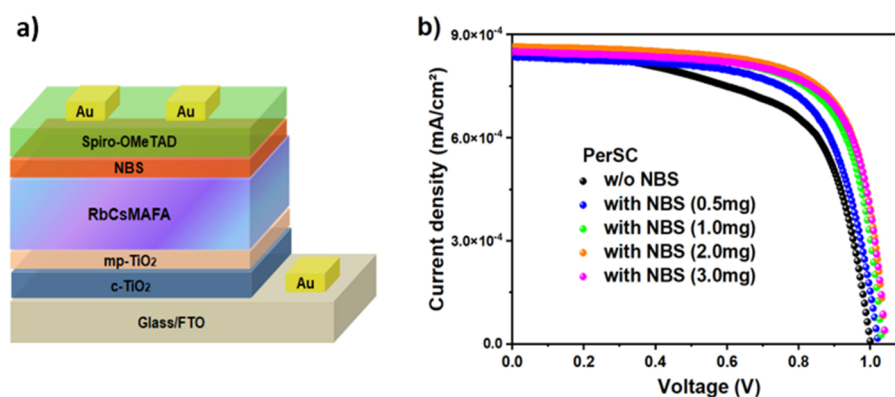


Figure 3. (a) n-i-p device architecture of the studied PerSCs, and (b) current density–voltage (J–V) curves of the corresponding PerSCs with and without NBS treatment.

To elucidate how the NBS interfacial layer influences charge transport dynamics in the devices, we performed electrochemical impedance spectroscopy (EIS) measurements under dark conditions. The Nyquist plots of the control and NBS-treated PerSCs (Figure 4a) exhibit two distinct semicircular arcs. The high-frequency arc corresponds to interfacial charge transfer, while the low-frequency arc reflects charge recombination within the device. They were fitted using the equivalent electrical circuit given in Figure 4a, which includes three resistances and two constant phase elements (CPEs) associated with carrier diffusion. In this model, R_s represents the series resistance from wires and contacts, R_{tr} denotes the charge transfer resistance, and R_{rec} is the charge recombination resistance. The associated capacitances include C_{HF} , which reflects the geometrical capacitance related to the intrinsic dielectric relaxation of the perovskite absorber, and C_{LF} , which originates from ionic accumulation at the perovskite/transport layer interfaces. These capacitances were extracted from the constant phase elements (CPEs) by applying Brug's protocol [47–49], and the corresponding values are summarized in Table S1. Analysis of the EIS parameters reveals that devices incorporating NBS exhibit lower R_{tr} values compared to the control devices (Figure 4b), indicating more efficient interfacial charge transfer from the perovskite to the HTL. At the same time, as shown in Figure 4c, NBS-treated devices display significantly higher R_{rec} across different applied bias voltages, suggesting that the NBS layer effectively suppresses non-radiative recombination. This dual effect is attributed to the passivation of interfacial defects by NBS molecules, which simultaneously coordinate with undercoordinated Pb^{2+} centers and compensate halide vacancies. Such passivation minimizes electronic trap states at the perovskite/HTL interface, thereby suppressing non-radiative recombination losses and promoting smoother charge transport. The EIS results confirm that the NBS interlayer facilitates faster charge transfer and enhances recombination resistance, consistent with the J–V data and responsible for the improved V_{oc} and PCE. The charge carrier lifetime (τ) was evaluated from the Bode plots (Figure S11) through the relation: $\tau = \frac{1}{2\pi f_p}$, where f_p represents the peak frequency associated with the charge transfer process at the perovskite/selective contacts interfaces [50]. The optimized device incorporating 2.0 mg/mL of NBS demonstrated an extended charge carrier lifetime of 1.82 μs , compared to 1.75 μs for the control device. This enhancement in carrier lifetime also indicates that NBS treatment effectively suppresses interfacial charge accumulation and minimizes non-radiative recombination pathways. Notably, the obtained value is consistent with those reported in previous interfacial engineering studies [51].

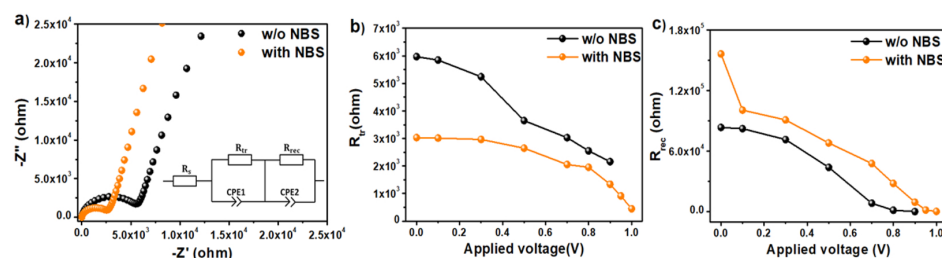


Figure 4. (a) Nyquist plots of the devices with and without NBS under dark conditions (the insert shows the equivalent circuit); applied bias-dependent (b) charge transfer resistance, and (c) charge recombination resistance extracted from EIS plots.

The Mott-Schottky (M-S) measurements are commonly employed in optoelectronic devices to evaluate the charge density profile of semiconductor junctions [52–55]. This analysis involves measuring the depletion layer capacitance, which arises from the change in charge occupation at the edge of the depletion zone of width (W). M-S measurements of the devices were conducted under dark conditions, and the results are shown in Figure 5. The M-S relationship is expressed by the equation [56,57]:

$$\frac{1}{C^2} = \frac{2}{\epsilon_0 \epsilon_r q N A^2} (V_{bi} - V)$$

where C is the capacitance, V_{bi} is the built-in potential, V is the applied voltage, q is the elementary charge (1.6×10^{-19} C), ϵ_0 is the vacuum permittivity (8.85×10^{-12} Fm $^{-1}$), ϵ_r is the relative permittivity (26.13), and N represents the doping density of immobile ions at depletion region (determined from the slope of the linear region). The built-in voltage can be determined from the x -axis intercept in the linear region and is found to be higher for the optimized device (1.02 V) compared to the control device without NBS (0.96 V), which follows the V_{oc} trend. This shows that NBS enhances the internal driving force for efficient charge carrier separation and transport. In general, the increased V_{bi} not only accelerates the dissociation of photo-generated carriers, but also favors the formation of an extended depletion region, thus reducing interfacial charge accumulation [58]. The depletion width (W) of the active layer was estimated using the equation $W = \sqrt{\frac{2\epsilon_0 \epsilon_r V_{bi}}{qN}}$. The results show that the depletion width increased from 63.12 nm in the control device without NBS to 74.85 nm in the device incorporating the NBS interfacial layer. This enlarged depletion region facilitates more efficient charge separation and suppresses non-radiative recombination losses, thereby contributing to the enhanced PV performance of the devices. Similarly to other succinimide-derived materials, NBS effectively passivates interfacial defects and suppresses non-radiative losses, demonstrating its strong potential for interfacial engineering in PerSCs [59,60].

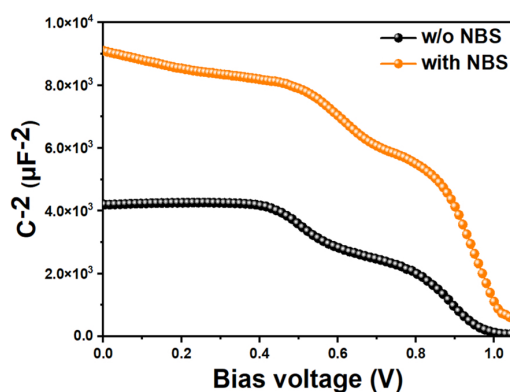


Figure 5. Mott-Schottky plot for the PerSCs with and without NBS.

4. Conclusions

In summary, we demonstrated an effective strategy to mitigate surface defects and control interfacial recombination through perovskite interface engineering with N-bromosuccinimide molecules. The effect of NBS concentration on the optoelectronic properties of quadruple cation perovskite films was systematically investigated, identifying 2.0 mg/mL as the optimal concentration. The carbonyl group in NBS passivates undercoordinated Pb^{2+} ions, while nitrogen–bromine bonds can inactivate defects related to halide vacancies through electrostatic interactions. This dual passivation reduces the defect states density on the perovskite film surface, resulting in greatly depressed non-radiative recombination losses and enhanced interfacial charge transfer between the RbCsMAFA perovskite and Spiro-OMeTAD. As a result, the PCE of the assembled devices increased from 16.48% for the control to 18.24% for the NBS-treated PerSCs, accompanied by a V_{oc} improvement from 1.004 V to 1.041 V. The charge dynamic properties of the devices were comprehensively investigated using electrochemical impedance spectroscopy. NBS treatment was found to reduce charge transfer resistance, increase recombination resistance, and prolong carrier lifetimes in the devices. Mott–Schottky analysis further showed that the depletion width increases from 63.12 nm to 74.85 nm, indicating enhanced interfacial quality and more efficient charge separation. In addition, the succinimide ring also provides a hydrophobic character, protecting the perovskite film from interaction with ambient moisture. Our study therefore provides deeper insight into defect passivation and perovskite/HTL interface engineering for the development of more efficient and stable PerSCs.

Supplementary Materials: The following supporting information can be downloaded at: <https://www.mdpi.com/article/10.3390/coatings15101195/s1>, Figure S1: UV-visible absorption spectra of N-bromosuccinimide (NBS) thin films coated on FTO glass substrates. Figure S2: Tauc plot of the RbCsMAFA perovskite films with and without NBS. Figure S3: SEM images of (a) pristine perovskite and (b) NBS-treated perovskite. Figure S4: Contact angle measurement on (a) pristine perovskite (PVK), (b) PVK/NBS (0.5 mg/mL), (c) PVK/NBS (1.0 mg/mL), (d) PVK/NBS (2.0 mg/mL), and (e) PVK/NBS (3.0 mg/mL). Figure S5: Photoluminescence spectra for untreated and NBS-treated perovskite films (2.0 mg/mL). Figure S6: X-ray photoelectron spectroscopy survey spectra of the perovskite films treated with different concentration of NBS. Figure S7: High-resolution X-ray photoelectron spectroscopy spectra of pristine PVK and NBS-treated PVK: (a) C 1s, (b) N 1s, (c) Pb 4f, (d) I 3d, (e) O 1s, (f) Br 3d, (g) Rb3d, and (h) Cs3d core levels. Figure S8: Cross-sectional SEM image of the fabricated PerSC with NBS. Figure S9: Reverse and forward scan *I*-*V* curves for the PerSC, (a) without NBS, (b) treated with NBS 0.5mg/mL, (c) 1.0 mg/mL, (d) 2.0 mg/mL, and (e) 3.0 mg/mL. Figure S10: Statistical distribution of V_{oc} , J_{sc} , PCE and FF, calculated on 8 PerSCs for each NBS concentration. Figure S11: Impedance spectroscopy Bode plots of the PerSCs with and without NBS. Table S1: Fitting parameters of the equivalent circuit model for different applied voltage for the PerSC (a) w/o NBS, and (b) with NBS (2.0 mg/mL).

Author Contributions: Conceptualization, H.D., R.C. and J.D.; Methodology, H.D.; Validation, H.D., P.C., G.S., W.B., A.B., G.H., F.L., and J.D.; Formal analysis, H.D.; Investigation, H.D., G.S., W.B., A.B., G.H. and F.L.; Resources, P.C., R.C. and J.D.; Writing—original draft, H.D.; Writing—review & editing, P.C., G.S., W.B., A.B., G.H., F.L., R.C. and J.D.; Visualization, H.D., and J.D.; Supervision, R.C. and J.D.; Project administration, P.C.; Funding acquisition, H.D., P.C. and J.D. All authors have read and agreed to the published version of the manuscript.

Funding: This work was supported by Wallonia-Brussels International (WBI) as part of an IN WBI excellence scholarship program awarded to H.D.

Data Availability Statement: The data presented in this study are available on request from the corresponding author.

Conflicts of Interest: The authors declare no conflict of interest.

References

- Kojima, A.; Teshima, K.; Shirai, Y.; Miyasaka, T. Organometal Halide Perovskites as Visible-Light Sensitizers for Photovoltaic Cells. *J. Am. Chem. Soc.* **2009**, *131*, 6050–6051. [\[CrossRef\]](#)
- Kim, H.S.; Lee, C.R.; Im, J.H.; Lee, K.B.; Moehl, T.; Marchioro, A.; Moon, S.J.; Baker, R.H.; Yum, J.H.; Moser, J.E.; et al. Lead Iodide Perovskite Sensitized All-Solid-State Submicron Thin Film Mesoscopic Solar Cell with Efficiency Exceeding 9%. *Sci. Rep.* **2012**, *2*, 591. [\[CrossRef\]](#)
- Wang, Q.; Tang, W.; Chen, Y.; Qiu, W.; Wu, Y.; Peng, Q. Over 25% efficiency and stable bromine-free RbCsFAMA-based quadruple cation perovskite solar cells enabled by an aromatic zwitterion. *J. Mater. Chem. A* **2023**, *11*, 1170–1179. [\[CrossRef\]](#)
- Zheng, Y.; Li, Y.; Zhuang, R.; Wu, X.; Tian, C.; Sun, A.; Chen, C.; Guo, Y.; Hua, Y.; Meng, K.; et al. Towards 26% efficiency in inverted perovskite solar cells via interfacial flipped band bending and suppressed deep-level traps. *Energy Environ. Sci.* **2024**, *17*, 1153–1162. [\[CrossRef\]](#)
- NREL, Best Research Cell Efficiencies Chart. Available online: <https://www.nrel.gov/pv/cell-efficiency.html> (accessed on 26 September 2024).
- Zhang, S.; Chen, R.; Qu, M.; Long, B.; He, N.; Huang, S.; Chen, X.; Li, H.; Xuan, T. Dual Strategy Based on Quantum Dot Doping and Phenylethylamine Iodide Surface Modification for High-Performance and Stable Perovskite Solar Cells. *Coatings* **2024**, *14*, 409. [\[CrossRef\]](#)
- Dhifaoui, H.; Hemasiri, N.H.; Aloui, W.; Bouazizi, A.; Kazim, S.; Ahmad, S. An approach to quantify the negative capacitance features in a triple-cation based perovskite solar cells. *Adv. Mater. Interfaces* **2021**, *8*, 2101002. [\[CrossRef\]](#)
- Daem, N.; Mayer, A.; Spronck, G.; Colson, P.; Loicq, J.; Henrist, C.; Cloots, R.; Maho, A.; Lobet, M.; Dewalque, J. Inverse Opal Photonic Nanostructures for Enhanced Light Harvesting in CH₃NH₃PbI₃ Perovskite Solar Cells. *ACS Appl. Nano Mater.* **2022**, *5*, 13583–13593. [\[CrossRef\]](#)
- Ding, Y.; Feng, X.; Feng, E.; Chang, J.; Li, H.; Long, C.; Gao, Y.; Lu, S.; Yang, J. Multi-Functional Regulation on Buried Interface for Achieving Efficient Triple-Cation Perovskite Solar Cells. *Small* **2024**, *20*, 2308836. [\[CrossRef\]](#) [\[PubMed\]](#)
- Dhifaoui, H.; Hemasiri, N.H.; Mehdi, H.; Bouazizi, A.; Kazim, S.; Ahmad, S. Impact of Polymeric Hole-Selective Layers on Chemical Inductance in Inverted Perovskite Solar Cells. *Energy Technol.* **2022**, *10*, 2200624. [\[CrossRef\]](#)
- Torres, J.; Zarazua, I.; Esparza, D.; Rivas, J.M.; Saliba, M.; Mora-Seró, I.; Turren-Cruz, S.H.; Abate, A. Degradation analysis of triple-cation perovskite solar cells by electrochemical impedance spectroscopy. *ACS Appl. Energy Mater.* **2022**, *5*, 12545–12552. [\[CrossRef\]](#)
- Ji, X.; Che, X.; Dai, W.; Gong, Y.; Zhang, Z.; Zhang, L.; Ma, C.; Yang, T.; Dong, Y.; Yan, B.; et al. Buried Interface Modification Using Diammonium Ligand Enhances Mechanical Durability of Flexible Perovskite Solar Cells. *Coatings* **2024**, *15*, 15. [\[CrossRef\]](#)
- Chen, Y.; Wang, Q.; Tang, W.; Qiu, W.; Wu, Y.; Peng, Q. Heterocyclic amino acid molecule as a multifunctional interfacial bridge for improving the efficiency and stability of quadruple cation perovskite solar cells. *Nano Energy* **2023**, *107*, 108154. [\[CrossRef\]](#)
- Tan, S.; Yavuz, I.; Weber, M.H.; Huang, T.; Chen, C.H.; Wang, R.; Wang, H.C.; Ko, J.H.; Nuryyeva, S.; Xue, J.; et al. Shallow iodine defects accelerate the degradation of α -phase formamidinium perovskite. *Joule* **2020**, *4*, 2426–2442. [\[CrossRef\]](#)
- Kim, H.; Yoo, S.M.; Ding, B.; Kanda, H.; Shibayama, N.; Syzgantseva, M.A.; Tirani, F.F.; Schouwink, P.; Yun, H.J.; Son, B.; et al. Shallow-level defect passivation by 6H perovskite polytype for highly efficient and stable perovskite solar cells. *Nat. Commun.* **2024**, *15*, 5632. [\[CrossRef\]](#) [\[PubMed\]](#)
- Boyd, C.C.; Cheacharoen, R.; Leijtens, T.; McGehee, M.D. Understanding degradation mechanisms and improving stability of perovskite photovoltaics. *Chem. Rev.* **2018**, *119*, 3418–3451. [\[CrossRef\]](#)
- Zhang, Z.; Qiao, L.; Meng, K.; Long, R.; Chen, G.; Gao, P. Rationalization of passivation strategies toward high-performance perovskite solar cells. *Chem. Soc. Rev.* **2023**, *52*, 163. [\[CrossRef\]](#) [\[PubMed\]](#)
- Zhang, J.; Mcgettrick, J.; Ji, K.; Bi, J.; Webb, T.; Liu, X.; Liu, D.; Ren, A.; Xiang, Y.; Li, B.; et al. Fast and balanced charge transport enabled by solution-processed metal oxide layers for efficient and stable inverted perovskite solar cells. *Energy Environ. Mater.* **2024**, *7*, e12595. [\[CrossRef\]](#)
- Obrero-Perez, J.M.; Contreras-Bernal, L.; Nuñez-Galvez, F.; Castillo-Seoane, J.; Valadez-Villalobos, K.; Aparicio, F.J.; Anta, J.A.; Borrás, A.; Sanchez-Valencia, J.R.; Barranco, A. Ultrathin plasma polymer passivation of perovskite solar cells for improved stability and reproducibility. *Adv. Energy Mater.* **2022**, *12*, 2200812. [\[CrossRef\]](#)
- Zhang, B.; Chen, C.; Wang, X.; Du, X.; Liu, D.; Sun, X.; Li, Z.; Hao, L.; Gao, C.; Li, Y.; et al. A multifunctional polymer as an interfacial layer for efficient and stable perovskite solar cells. *Angew. Chem. Int. Ed.* **2023**, *62*, e202213478. [\[CrossRef\]](#)
- Lian, S.; Liu, M.; Zhu, H.; Wu, Y.; Dolgoma, A.; Zhang, Y.; Zhan, H.; Liu, J.; Wang, L.; Qin, C. Multifunctional BODIPY-Structured n-Type Conjugated Polymer for Simultaneous Interface Energetic Modification and Defect Passivation to Boost Efficiency and Stability of Inverted Perovskite Solar Cells. *J. Phys. Chem. Lett.* **2025**, *16*, 4835. [\[CrossRef\]](#)
- Salado, M.; Jodlowski, A.D.; Roldan-Carmona, C.; de Miguel, G.; Kazim, S.; Nazeeruddin, M.K.; Ahmad, S. Surface passivation of perovskite layers using heterocyclic halides: Improved photovoltaic properties and intrinsic stability. *Nano Energy* **2018**, *50*, 220. [\[CrossRef\]](#)

23. Li, S.; Wu, Y.; Zhang, C.; Liu, Y.; Sun, Q.; Cui, Y.; Liu, S.F.; Hao, Y. Interface modification of a perovskite/hole transport layer with tetraphenyldibenzoperiflanthene for highly efficient and stable solar cells. *ACS Appl. Mater. Interfaces* **2020**, *12*, 45073–45082. [[CrossRef](#)] [[PubMed](#)]
24. Dong, Z.; Men, J.; Zhang, B.; Xie, X.; Huang, Z.; Ma, Z.; Zhai, Z.; Wang, Y.; Zeng, Y.; Wu, J.; et al. Grain Boundary Defect Passivation and Iodine Migration Inhibition for Efficient and Stable Perovskite Solar Cells. *Electrochim. Acta* **2024**, *507*, 145129. [[CrossRef](#)]
25. Cheng, H.; Zang, X.; Wang, S.; Cai, B. Pyridine-Functionalized Organic Molecules in Perovskite Solar Cells: Toward Defects Passivation and Charge Transfer. *Sol. RRL* **2025**, *9*, 2400736. [[CrossRef](#)]
26. Zhu, H.; Liu, Y.; Eickemeyer, F.T.; Pan, L.; Ren, D.; Ruiz-Preciado, M.A.; Carlsen, B.; Yang, B.; Dong, X.; Wang, Z.; et al. Tailored amphiphilic molecular mitigators for stable perovskite solar cells with 23.5% efficiency. *Adv. Mater.* **2020**, *32*, 1907757. [[CrossRef](#)]
27. Hemasiri, N.H.; Kazim, S.; Ahmad, S. Reduced trap density and mitigating the interfacial losses by placing 2D dichalcogenide material at perovskite/HTM interface in a dopant free perovskite solar cells. *Nano Energy* **2020**, *77*, 105292. [[CrossRef](#)]
28. Daem, N.; Dewalque, J.; Kim, D.K.; Spronck, G.; Attwood, M.; Wade, J.; Henrist, C.; Colson, P.; Heutz, S.; Cloots, R.; et al. Improved Photovoltaic Performances of Lead-Free Cs₂AgBiBr₆ Double Perovskite Solar Cells Incorporating Tetracene as Co-Hole Transport Layer. *Sol. RRL* **2023**, *7*, 2300391. [[CrossRef](#)]
29. Wang, P.; Liu, J.; Shang, W.; Xu, T.; Wang, M.; Shi, Y.; Cai, R.; Bian, J. Rational selection of the lewis base molecules targeted for lead-based defects of perovskite solar cells: The synergetic co-passivation of carbonyl and carboxyl groups. *J. Phys. Chem. Lett.* **2023**, *14*, 653. [[CrossRef](#)]
30. Guo, M.; Chen, Y.; Chen, S.; Zuo, C.; Li, Y.; Chang, Y.J.; Li, J.; Wei, M. Synchronous effect of coordination and hydrogen bonds boosting the photovoltaic performance of perovskite solar cells. *Electrochim. Acta* **2024**, *492*, 144335. [[CrossRef](#)]
31. Manjunath, S.B.; Soe, K.T.; Supasai, T.; Rujisamphan, N.; Devadiga, D.; Nagaraja, A.T. Nonbonding electron pairs in cyano and carbonyl groups act as defect passivation in hybrid perovskite solar cells. *ACS Appl. Energy Mater.* **2024**, *7*, 10294. [[CrossRef](#)]
32. Fang, Z.; Gillatt, R.Z.; Slawin, A.M.; Cordes, D.B.; Carpenter-Warren, C.L.; O'Hagan, D. Unexpected α, α' -difluoroethers from Ag(i)F and N-bromosuccinimide reactions of dibenzo[a,e]cyclooctatetraene. *Chem. Commun.* **2019**, *55*, 14295–14298. [[CrossRef](#)]
33. Pan, S.; Yang, X.; Cai, B.; Yang, K.; Ge, M.; Zhang, T.; Cui, H.; Sunab, L.; Ji, W. N-Bromosuccinimide as a p-type dopant for a Spiro-OMeTAD hole transport material to enhance the performance of perovskite solar cells. *Sustain. Energy Fuels* **2021**, *5*, 2294–2300. [[CrossRef](#)]
34. Ding, Y.; Ding, B.; Kanda, H.; Usiobo, O.J.; Gallet, T.; Yang, Z.; Liu, Y.; Huang, H.; Sheng, J.; Liu, C.; et al. Single-crystalline TiO₂ nanoparticles for stable and efficient perovskite modules. *Nat. Nanotechnol.* **2022**, *17*, 598–605. [[CrossRef](#)]
35. García-Rodríguez, R.; Ferdani, D.; Pering, S.; Baker, P.J.; Cameron, P.J. Influence of bromide content on iodide migration in inverted MAPb (I_{1-x}Br_x)₃ perovskite solar cells. *J. Mater. Chem. A* **2019**, *7*, 22604–22614. [[CrossRef](#)]
36. Gupta, R.K.; Garai, R.; Hossain, M.; Choudhury, A.; Iyer, P.K. Dual-Passivation Strategy for Improved Ambient Stability of Perovskite Solar Cells. *ACS Sustain. Chem. Eng.* **2021**, *9*, 7993–8001.
37. Liu, Y.; Xiang, W.; Mou, S.; Zhang, H.; Liu, S. Synergetic surface defect passivation towards efficient and stable inorganic perovskite solar cells. *Chem. Eng. J.* **2022**, *447*, 137515. [[CrossRef](#)]
38. Kurahashi, N.; Runkel, M.; Kreusel, C.; Schiffer, M.; Maschwitz, T.; Kraus, T.; Brinkmann, K.O.; Heiderhoff, R.; Buchmüller, M.; Schumacher, S.O.; et al. Distributed Feedback Lasing in Thermally Imprinted Phase-Stabilized CsPbI₃ Thin Films. *Adv. Funct. Mater.* **2024**, *34*, 2405976. [[CrossRef](#)]
39. Wang, S.; Cao, F.; Wu, Y.; Zhang, X.; Zou, J.; Lan, Z.; Sun, W.; Wu, J.; Gao, P. Multifunctional 2D perovskite capping layer using cyclohexylmethylammonium bromide for highly efficient and stable perovskite solar cells. *Mater. Today Phys.* **2021**, *21*, 100543. [[CrossRef](#)]
40. Abate, S.Y.; Jha, S.; Shaik, A.K.; Ma, G.; Emodogo, J.; Pradhan, N.; Gu, X.; Patton, D.; Hammer, N.I.; Dai, Q. Fabrication of 1D/3D heterostructure perovskite layers by tetrabutylammonium tetrafluoroborate for high-performance devices. *Org. Electron.* **2024**, *125*, 106984. [[CrossRef](#)]
41. Lee, J.W.; Tan, S.; Seok, S.I.; Yang, Y.; Park, N.G. Rethinking the A cation in halide perovskites. *Science* **2022**, *375*, eabj1186. [[CrossRef](#)]
42. Zheng, X.; Chen, B.; Dai, J.; Fang, Y.; Bai, Y.; Lin, Y.; Wei, H.; Zeng, X.C.; Huang, J. Defect passivation in hybrid perovskite solar cells using quaternary ammonium halide anions and cations. *Nat. Energy* **2017**, *2*, 17102. [[CrossRef](#)]
43. Singh, H.; Fei, R.; Rakita, Y.; Kulbak, M.; Cahen, D.; Rappe, A.M.; Frenkel, A.I. Origin of the anomalous Pb-Br bond dynamics in formamidinium lead bromide perovskites. *Phys. Rev. B* **2020**, *101*, 054302. [[CrossRef](#)]
44. Gao, X.X.; Ding, B.; Zhang, Y.; Zhang, S.; Turnell-Ritson, R.C.; Kanda, H.; Abuhelaiqa, M.; Shibayama, N.; Luo, W.; Li, M.; et al. Halide exchange in the passivation of perovskite solar cells with functionalized ionic liquids. *Cell Rep. Phys. Sci.* **2022**, *3*, 100848. [[CrossRef](#)]
45. Courtier, N.E.; Cave, J.M.; Foster, J.M.; Walker, A.B.; Richardson, G. How transport layer properties affect perovskite solar cell performance: Insights from a coupled charge transport/ion migration model. *Energy Environ. Sci.* **2019**, *12*, 396–409. [[CrossRef](#)]

46. Brug, G.J.; Van Der Eeden, A.L.G.; Sluyters-Rehbach, M.; Sluyters, J.H. The analysis of electrode impedances complicated by the presence of a constant phase element. *J. Electroanal. Chem.* **1984**, *176*, 275–295. [\[CrossRef\]](#)
47. Ulfa, M.; Zhu, T.; Goubard, F.; Pauporté, T. Molecular versus polymeric hole transporting materials for perovskite solar cell application. *J. Mater. Chem. A* **2018**, *6*, 13350–13358. [\[CrossRef\]](#)
48. Jacobs, D.A.; Shen, H.; Pfeffer, F.; Peng, J.; White, T.P.; Beck, F.J.; Catchpole, K.R. The two faces of capacitance: New interpretations for electrical impedance measurements of perovskite solar cells and their relation to hysteresis. *J. Appl. Phys.* **2018**, *124*, 225702. [\[CrossRef\]](#)
49. Srivastava, V.; Alexander, A.; Anitha, B.; Namboothiry, M.A. Impedance spectroscopy study of defect/ion mediated electric field and its effect on the photovoltaic performance of perovskite solar cells based on different active layers. *Sol. Energy Mater. Sol. Cells* **2022**, *237*, 111548. [\[CrossRef\]](#)
50. Kumar, Y.; Regalado-Perez, E.; Jerónimo-Rendón, J.J.; Mathew, X. Effect of Cs⁺ and K⁺ incorporation on the charge carrier lifetime, device performance and stability in perovskite solar cells. *Sol. Energy Mater. Sol. Cells* **2022**, *236*, 111512. [\[CrossRef\]](#)
51. Tang, J.; Liu, L.; Yu, Z.; Du, J.; Cai, X.; Zhang, M.; Zhao, M.; Bai, L.; Gai, Z.; Cui, S.; et al. Interfacial Modification by Low-Temperature Anchoring of Surface Uncoordinated Pb for Efficient FAPbI₃ Perovskite Solar Cells. *Adv. Sustain. Syst.* **2022**, *6*, 2100510. [\[CrossRef\]](#)
52. Gelderman, K.; Lee, L.; Donne, S.W. Flat-band potential of a semiconductor: Using the Mott–Schottky equation. *J. Chem. Educ.* **2007**, *84*, 685. [\[CrossRef\]](#)
53. Almora, O.; Aranda, C.; Mas-Marzá, E.; Garcia-Belmonte, G. On Mott-Schottky analysis interpretation of capacitance measurements in organometal perovskite solar cells. *Appl. Phys. Lett.* **2016**, *109*, 173903. [\[CrossRef\]](#)
54. Fischer, M.; Tvingstedt, K.; Baumann, A.; Dyakonov, V. Doping profile in planar hybrid perovskite solar cells identifying mobile ions. *ACS Appl. Energy Mater.* **2018**, *1*, 5129–5134. [\[CrossRef\]](#)
55. Guerrero, A.; Bisquert, J.; Garcia-Belmonte, G. Impedance spectroscopy of metal halide perovskite solar cells from the perspective of equivalent circuits. *Chem. Rev.* **2021**, *121*, 14430–14484. [\[CrossRef\]](#)
56. Ghahremanirad, E.; Almora, O.; Suresh, S.; Drew, A.A.; Chowdhury, T.H.; Uhl, A.R. Beyond protocols: Understanding the electrical behavior of perovskite solar cells by impedance spectroscopy. *Adv. Energy Mater.* **2023**, *13*, 2204370. [\[CrossRef\]](#)
57. Ravishankar, S.; Liu, Z.; Rau, U.; Kirchartz, T. Multilayer capacitances: How selective contacts affect capacitance measurements of perovskite solar cells. *PRX Energy* **2022**, *1*, 013003. [\[CrossRef\]](#)
58. Elbohy, H.; Suzuki, H.; Nishikawa, T.; Kyaw, A.K.K.; Hayashi, Y. Phenolphthalein: A Potent Small-Molecule Additive for High-Performance and Ambient-Air-Stable FAPbI₃ Perovskite Solar Cells. *ACS Appl. Energy Mater.* **2024**, *7*, 2925–2937. [\[CrossRef\]](#)
59. Zhang, Y.; Wang, Y.; Ma, Y.; Liu, R.; Li, L.; Zhang, N.; Xing, Z.; Mao, X.; Xi, X.; Wang, P.; et al. Introduction of N-hydroxy succinimide to improve overall efficiency and stability of perovskite solar cells. *Appl. Surf. Sci.* **2025**, 163916. [\[CrossRef\]](#)
60. Kozlov, S.S.; Alexeeva, O.V.; Nikolskaia, A.B.; Petrova, V.I.; Karyagina, O.K.; Iordanskii, A.L.; Larina, L.L.; Shevaleevskiy, O.I. Defect Passivation in Perovskite Solar Cells Using Polysuccinimide-Based Green Polymer Additives. *Polymers* **2025**, *17*, 653. [\[CrossRef\]](#)

Disclaimer/Publisher’s Note: The statements, opinions and data contained in all publications are solely those of the individual author(s) and contributor(s) and not of MDPI and/or the editor(s). MDPI and/or the editor(s) disclaim responsibility for any injury to people or property resulting from any ideas, methods, instructions or products referred to in the content.